iScience

CellPress
OPEN ACCESS

Article

Steam condensation heat transfer on lubricant-infused surfaces

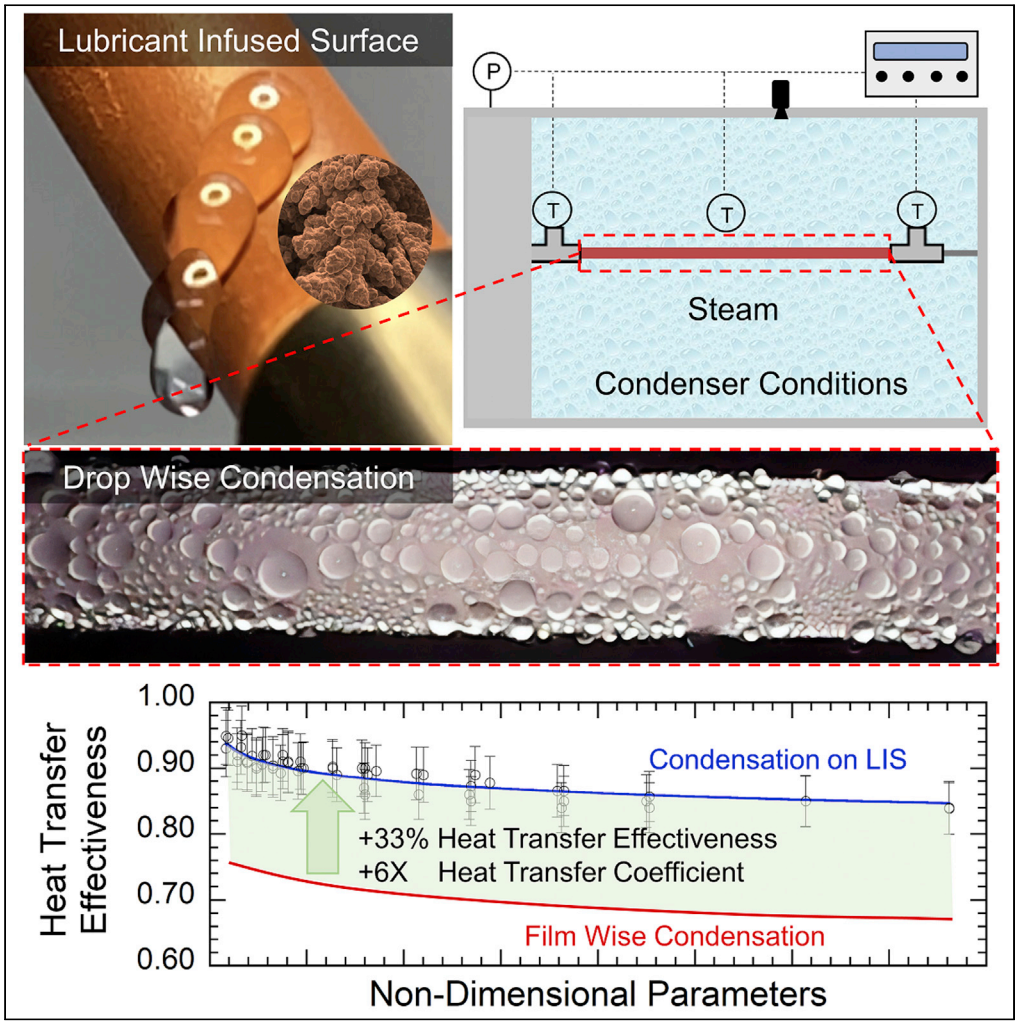

Ryan Stoddard, Karthik Nithyanandam, Ranga Pitchumani

pitchu@vt.edu

Highlights

Presents condensation heat transfer enhancement using liquid infused surfaces

Studies conducted in a typical power plant condenser environment

Results quantified using heat transfer effectiveness for a system perspective

Analytical relationships derived for LIS heat transfer effectiveness and durability

Stoddard et al., iScience *24*, 102336
April 23, 2021
https://doi.org/10.1016/j.isci.2021.102336

iScience

CellPress
OPEN ACCESS

Article

Steam condensation heat transfer on lubricant-infused surfaces

Ryan Stoddard,[1] Karthik Nithyanandam,[1] and Ranga Pitchumani[1,2,*]

SUMMARY

Steam condensation is fundamental to several industrial processes, including power generation, desalination, and water harvesting. Lubricant-infused surfaces (LISs) promote sustained dropwise condensation, leading to significantly higher heat transfer performance that trades off with durability. Here, we present a systematic study on lubricant-infused copper tubes in a partial vacuum environment typical of power plant condensers to elucidate the influence of the design parameters—texturing, functionalizing agent, and lubricant viscosity—on condensation heat transfer performance and durability. Heat transfer effectiveness is introduced as a relevant parameter to quantify the effects of condensation heat transfer coefficient enhancement on the overall system heat transfer performance. Analytical expressions are developed for lubricant retention fraction and heat transfer effectiveness in terms of Bond number, viscosity ratio, and a dimensionless logarithmic mean temperature difference that can be used for predicting the performance of a LIS or for designing surfaces for a desired performance.

INTRODUCTION

Condensation of steam plays a significant role in various industrial processes (Liu and Preston, 2019), including desalination (Bilgil and Hırlakoğlu, 2017; Cao et al., 2020; Huang et al., 2020); power generation (Bao et al., 2017; Chuang and Sue, 2005; Yang et al., 2019); water harvesting (Jarimi et al., 2020); and heating, ventilation, and air conditioning systems (Brenner et al., 2020; Wang et al., 2020). Of significance for this study, steam cycle efficiency is directly tied to condensation heat transfer effectiveness in a power plant condenser. Any sustainable improvement to condenser effectiveness on an industrial scale can lead to significant gains in efficiency for power generation worldwide.

Steam condensation occurs when water vapor contacts a surface whose temperature is below the dewpoint for the operating pressure, thus causing liquid droplets to form on the surface. The temperature difference between the condensing surface and the vapor is referred to as the degree of subcooling. Typical power plant condensers operate with a degree of subcooling range of about 6–11°C (Guyer, 2013). For most industrial applications, the condensing liquid quickly forms a thin condensate layer that covers the condensing surface. Since the thermal conductivity of water is substantially lower than most metals, this resulting film-wise condensation (FWC) layer creates a constant, undesirable thermal resistance barrier to steady state condensation heat transfer (Rose, 1988). Conversely, dropwise condensation (DWC) is characterized by droplets of condensate shedding from the condensing surface quickly after forming, thus leaving a substantial amount of the surface available for additional condensing droplets. The condensation heat transfer coefficients obtained from DWC are typically an order of magnitude larger than those for FWC (Tanner et al., 1965), making DWC a preferred mode of condensation heat transfer.

Lubricant-infused surfaces (LISs) have shown promise in promoting sustained DWC (Attinger et al., 2014) due to extremely low adhesion between the condensing liquid and the infused lubricant leading to droplet self-removal at inclination angles as low as 5° (Wong et al., 2013). An LIS is fabricated by first creating nano- or micro-scale roughness on a substrate surface, then functionalizing the resulting surface with a chemical that lowers the surface energy of the textured surface, and finally infusing a lubricant into the textured surface to provide a hybrid, lubricant-solid interface between the substrate and the surrounding environment (Preston et al., 2017). Various means of surface texturing have been used for LIS preparation, including deposition of carbon nanotubes (Rungraeng et al., 2015), chemical etching (Wang et al., 2016), and carving of regular pillars (Anand et al., 2012; Preston et al., 2017). However, the nanopatterning methods are not

[1]Advanced Materials and Technologies Laboratory, Department of Mechanical Engineering, Virginia Tech, Blacksburg, VA 24061-0238, USA

[2]Lead contact

*Correspondence: pitchu@vt.edu

https://doi.org/10.1016/j.isci.2021.102336

scalable to large, practical surfaces such as condenser tubes that are widely used in industries. Recent trends have tended toward non-metallic substrates (Villegas et al., 2019), that are also not suitable for condensation heat transfer applications.

Nearly all studies in the literature on LIS use a derivative of silane as the functionalizing agent after substrate texturing (Anand et al., 2012; Preston et al., 2018; Preston et al., 2017; Rungraeng et al., 2015; Schellenberger et al., 2015; Shi et al., 2017; Tsuchiya et al., 2017; Wang et al., 2016). Different fluids have been infused to make LISs, including fluorinated electronic liquids (Schellenberger et al., 2015), silicone oil (Tsuchiya et al., 2017), and ionic fluids (Anand et al., 2012), but most efforts focus on perfluoropolyether (PFPE) lubricants (Shi et al., 2017). The PFPE lubricants used in the literature show the most promise in both heat transfer enhancement and durability. Often, however, a particular study will focus on a single lubricant, such as Krytox 101, with little description of the lubricant selection process or comparison with alternatives, specifically in relation to lubricant viscosity. Likewise, heat transfer enhancement using LIS and associated durability challenges have been observed without exploration of the parameters leading to lubricant depletion (Preston et al., 2018).

In the literature, condensation heat transfer improvements from surface modifications are typically quantified in terms of increase in condensation heat transfer coefficient (Wen et al., 2018; Zhang et al., 2020) or heat flux (Preston et al., 2018; Wen et al., 2018; Zhang et al., 2020). Although heat transfer coefficient is a relevant fundamental parameter, it does not provide any insight into its consequence on the system level performance, which can result in ambiguous interpretations. As a parameter, heat transfer coefficient ranges in scale from zero to infinity, with the implication that large improvements will translate to an equivalent increase in heat transfer from the modified surface. This implication, however, ignores that the modified surface is part of a larger heat transfer system whose overall heat transfer is governed by resistances from several other modes of thermal transport and can only be improved by a finite amount. For instance, in the case of a water-cooled condenser, above a certain value of condensation heat transfer coefficient, the limiting thermal resistance of the system quickly shifts to either forced convection of the cooling water on the interior of the condenser tubes or conduction through the tube wall. For this reason, heat transfer from the system cannot approach infinity, even if extremely large values of heat transfer coefficient can be achieved on the condensing surface. The alternative approach of quantifying improvements in terms of heat flux also suffers from the same limitation of lacking a context to a theoretical, maximum level of heat transfer that can be achieved by improvement of the condensing surface alone, rendering the numbers difficult to interpret across non-wetting surface designs.

It is evident from the foregoing discussion that there has been a flurry of recent literature on condensation heat transfer on LISs. While the general theme of the publications is that of reporting different methods of fabrication and associated condensation heat transfer measurements depicting large heat transfer coefficient values, there has been little context on the implications of the large numbers or the trade-offs between heat transfer improvement and surface durability. For example, are such large heat transfer coefficients really necessary? Do they translate proportionally to heat transfer enhancement in actual systems? Are the fabrication methods scalable to real systems? Is full lubricant retention imperative for durability of heat transfer performance? The present work addresses these questions and provides several major contributions to the field of condensation heat transfer on LISs, as highlighted below.

1. The study, for the first time, explores and quantifies the influence of surface texturing, functionalizing agent, and lubricant selection on condensation heat transfer performance and durability of copper-based LISs through systematic experimental investigations. A facile surface texturing method is presented, whereby metallic tubes are textured to create multiscale asperities using electrodeposition or chemical etching, both widely used methods in practice, to overcome the shortcomings of nanopatterning method that is often studied in the literature.
2. The heat transfer results obtained from the experiments are quantified in terms of both heat transfer coefficient for fundamental description and heat transfer effectiveness that represents a unified way of reporting condensation heat transfer enhancement on LISs from an applied perspective. The use of a heat transfer effectiveness eliminates the limitations of conventional approaches to quantifying the enhancement in terms of the heat transfer coefficient or the heat flux alone and allows for a holistic understanding of system improvements stemming from increased surface condensation heat transfer. Through systematic studies, it is shown that the least amount of lubricant that maintains

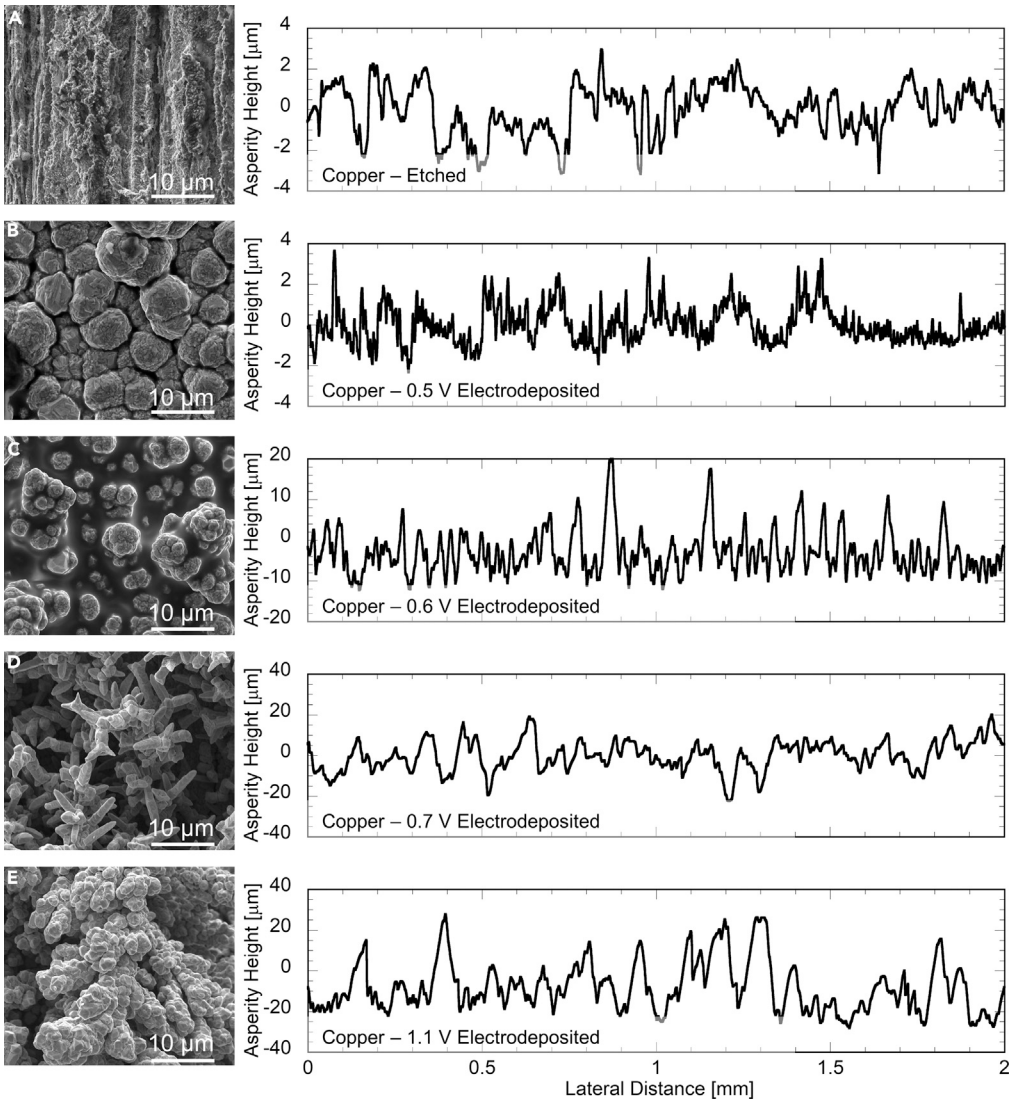

Figure 1. SEM micrographs and surface profiles of textured copper tubes

SEM micrographs and surface profilometry scans of (A) etched copper tube; (B) 0.5V electrodeposited copper tube; (C) 0.6V electrodeposited copper tube; (D) 0.7V electrodeposited copper tube; and (E) 1.1V electrodeposited copper tube. Scale bar size is 10 μm.

dropwise condensation is sufficient for achieving maximum heat transfer effectiveness. This finding is significant as lubricant drainage is often stated as a limitation of LISs, whereas the study finds that LISs could have high performance despite some drainage.

3. A fundamental, non-dimensional correlation for lubricant retention fraction and heat transfer effectiveness as a function of Bond number, a viscosity ratio and a dimensionless logarithmic mean temperature difference is developed that can be used to design liquid-infused surfaces for water-cooled surface condensers.

RESULTS AND DISCUSSION

Surface texturing: morphology and dimensions

Figure 1 shows the topography of copper test section surfaces textured using five different fabrication techniques. Each of the test section surface texturing methods yielded a distinct microstructure and surface

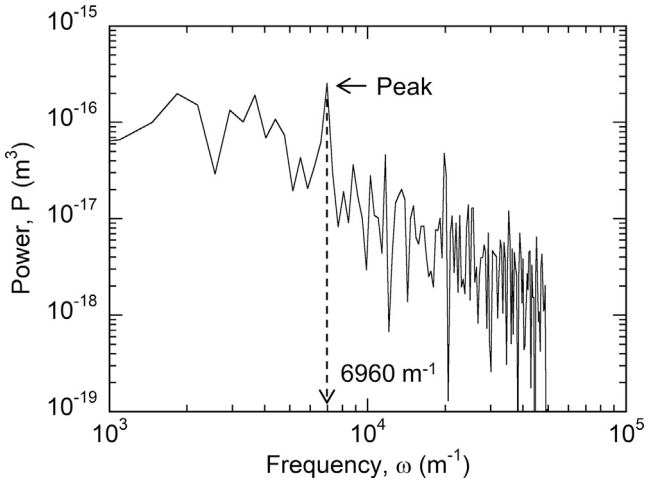

Figure 2. Fast-Fourier transform of etched copper tube surface profile showing power spike at 6,960 m^{-1}

profile. As shown in Figure 1A, the etched surface displayed an irregular microstructure with an asperity height of ±3 μm. The 0.5 V (Figures 1B) and 0.6 V (Figure 1C) electrodeposited surfaces exhibit boulderlike microstructure with asperity heights predominantly ranging between ±3 μm and ±15 μm, respectively. The 0.7 V (Figure 1D) electrodeposited surface had a needlelike microstructure with an asperity height of ±20 μm and the 1.1 V (Figure 1E) electrodeposited surface had a cauliflower-like microstructure with asperity height varying between ±24 μm.

The surfaces were quantitatively defined by two dimensional characteristics: peak-to-valley asperity height (a) and mean peak spacing (s). The peak-to-valley asperity heights of the etched, 0.5 V, 0.6 V, 0.7 V, and 1.1 V electrodeposited surfaces were 6.20 μm, 6.69 μm, 30.70 μm, 40.02 μm, and 47.68 μm, respectively. The mean peak spacing of asperity (s) for the various surfaces was determined using Fast-Fourier Transform (FFT) analysis. Specifically, the FFT of the surface profile for each finish was evaluated for a power spike. An example FFT of etched copper tube surface is shown in Figure 2. As shown in Figure 2, the power spike for this etched surface occurred at 6,960 m^{-1}, corresponding to s of 143.7 μm. Performing this analysis on five test section surfaces for each texturing method showed that the etched, 0.5 V, 0.6 V, 0.7 V, and 1.1 V electrodeposited surfaces had s values of 133.7 μm, 186.3 μm, 79.0 μm, 60.7 μm, and 101.3 μm, respectively. The characteristic dimensions of the tested surface textures along with standard deviation estimates are summarized in Table 1.

Heat transfer effectiveness

The condensation heat transfer coefficient (h_c) can vary from zero to infinity, making it unwieldy in evaluating the actual effectiveness of a modified surface in a heat transfer circuit. Specifically, the data reduction techniques used in the literature (Panuthara et al., 2019; Preston et al., 2015; Zhang et al., 2020) and in this study to derive h_c can lead to exceedingly large values and uncertainty bands, particularly at low logarithmic mean temperature difference (ΔT_{LM}), with little reference to actual improvement of heat transfer performance of the system. The effectiveness of a heat exchanger is described as the ratio of the real heat transfer rate to the maximum possible heat transfer rate of the heat exchanger (Haseli et al., 2008), and is used for heat exchanger design and optimization (Fakheri, 2007; Pattanayak et al., 2019). The use of the heat transfer effectiveness reduces ambiguity of results presented in terms of h_c or q'' alone, and highlights the overall improvement in system performance achieved through enhanced condenser surfaces.

For any fixed coolant flow rate and condenser material setup, the inner forced convection resistance to heat transfer (R_i) and tube wall material resistance to heat transfer (R_m) are known, allowing calculation of a maximum attainable heat flux (q''_{max}) through the external surface. At q''_{max}, h_c is theoretically infinite and the external condensation resistance to heat transfer (R_e) is consequently zero, which can be expressed as:

$$q''_{max} = \frac{\Delta T_{LM}}{A_s(R_i + R_m)} \quad \text{(Equation 1)}$$

Table 1. Physical characteristics (and uncertainty) of substrate texturing

Texturing	a (μm)	s (μm)	V_L^0 (μL)
Etched	6.20 (0.45)	133.7 (17.3)	15.46 (0.58)
0.5 V electrodeposited	6.69 (0.81)	186.3 (7.5)	16.69 (0.52)
0.6 V electrodeposited	30.70 (0.97)	79.0 (13.5)	76.57 (1.52)
0.7 V electrodeposited	40.02 (0.66)	60.7 (6.7)	99.82 (1.11)
1.1 V electrodeposited	47.68 (1.29)	101.3 (16.0)	118.92 (1.74)

in which A_s is the outer surface area of the test section. The q''_{max} can now be used to gauge the effectiveness, ε, of any surface modification using the following equation

$$\varepsilon = \frac{q''}{q''_{max}} = \frac{R_i + R_m}{R_i + R_m + R_e} \quad \text{(Equation 2)}$$

where q'' is the experimentally measured heat flux and ε is heat transfer effectiveness.

Figures 3A and 3B show plots of ε against h_c assuming various metal substrates with different thermal conductivities (k_m) and various coolant flow rates for the condenser test apparatus used in this study. The inner surface forced convection resistance, R_i, is based on interior tube roughness and cooling water Reynolds number (Re_i) and is constant for a steady state operational system. For the experimental setup in this study, the interior tube walls were smooth and the coolant Re_i averaged approximately 13,000, yielding an R_i of about 31.6°C/kW for the curves in Figure 3A. Further, for a generalized applicability across different tube materials, the tube wall thermal conductivity, k_m (which relates to R_m), was varied to demonstrate its effect on the variation of ε with the condensation heat transfer coefficient, as presented in Figure 3A. With known R_i and R_m, h_c was varied from 0 to 100 kW/m^2-°C (consequently varying R_e from infinity to 2°C/kW) to determine ε for each curve. For reference, the blue-shaded region in Figures 3A and 3B shows the expected range of heat transfer coefficients for FWC on a single tube based on Nusselt correlation (Nusselt, 1916). Figure 3B shows the effect of varying coolant Re_i while maintaining a constant k_m, that of copper.

Figures 3A and 3B reveal at least five useful findings. First, for Reynolds number of 13,000, FWC can achieve ε of roughly 70% on copper tubes (Figure 3A). So, a steady state system can only improve by about 30 percentage points even if the condensing surface achieves h_c of infinity. This maximum ε improvement reduces as k_m of the condensing surface decreases because of the increased thermal resistance offered by low conductivity tube material. Figure 3B shows that the effectiveness corresponding to the FWC heat transfer coefficient of 15 kW/m^2-°C increases with decrease in coolant flow Reynolds number from ε = 0.62 for Re_i = 20,000 to ε = 0.85 for Re_i = 5,000. Hence, the achievable percentage improvement gains through enhancement in condensation heat transfer coefficient from the baseline value for FWC diminishes with decrease in coolant flow Reynolds number. Second, the percentage increase in ε is not directly proportional to the percentage increase in h_c. In Figure 3A, a 120% increase in h_c on a copper surface from 25 kW/m^2°C to 55 kW/m^2°C only results in a 10% increase in ε. Thus, ε gives a much more realistic understanding of the actual thermal enhancement to the system provided by an improvement in condensation heat transfer than h_c, particularly in heat exchanger systems where the condensing surface temperature cannot be controlled directly. Third, the thermal conductivity (k_m) of the tube material makes very little impact on the shape of the ε curve. Comparing the results obtained for copper (k_m = 385 W/m-°C) and Hastelloy (k_m = 12 W/m-°C) in Figure 3A, a higher effectiveness value is achieved at lower values of h_c for low thermal conductivity substrates. Fourth, decreasing coolant Re_i reduces the effect of h_c on the ε curve. Focusing on the Re_i: 15,000 curve (Figure 3B), the condensation heat transfer is the limiting thermal resistance in the system up until approximately 20 kW/m^2-°C as observed from the linear increase in ε. From 20 kW/m^2-°C to 60 kW/m^2-°C, the resistances of condensation heat transfer and internal convection heat transfer are roughly equivalent. Above 60 kW/m^2-°C, internal convection heat transfer is clearly the dominant thermal resistance in the system as demonstrated by the asymptotic behavior of the ε curve. Finally, h_c values above approximately 100 kW/m^2-°C contribute to an insignificant improvement in an industrial heat transfer system since ε is already above 0.90 and is in the asymptotic regime (Figure 3). For systems constructed of materials with lower thermal conductivity, effectiveness of 0.95 is achieved at h_c closer to 70 kW/m^2-°C (Figure 3A). Overall, presenting heat transfer results in terms of ε allows appropriate

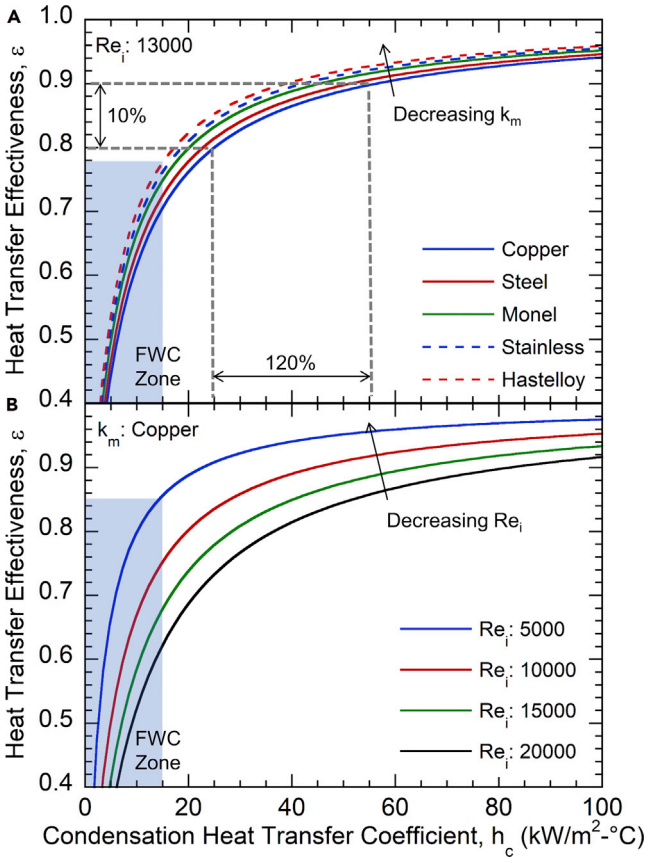

Figure 3. Heat transfer effectiveness as a function of condensation heat transfer coefficient

Heat transfer effectiveness as a function of condensation heat transfer coefficient for (A) various metal condensing surfaces and (B) various coolant Reynolds numbers.

context for improvements in heat transfer performance by considering both the maximum attainable heat flux and the constraints of the heat transfer circuit of the condenser system under study.

Parametric study

There are three essential design components that must be considered with an LIS: texturing, functionalizing agent, and infused lubricant. Three series of experiments were conducted in the test apparatus described in transparent methods (supplemental information; Figure S1; Table S1) to analyze the effect on heat transfer characteristics and retained lubricant (V_L) due to the variation of a single design parameter in each test series. As shown in Table 2, texturing was varied while functionalizing agent and infused lubricant were held constant for the first test series; functionalizing agent was varied while texturing and infused lubricant were held constant for the second test series; and infused lubricant was varied while texturing and functionalizing agent were held constant for the third test series. Additionally, heat transfer performance was referenced to the classic Nusselt correlation (Nusselt, 1916) for FWC (h_{Nu}) on a single tube to determine the baseline for improvements:

$$h_{Nu} = 0.729\left[\frac{g\rho_l(\rho_l-\rho_v)k_l^3\lambda_{fg}}{\mu_l D_o \Delta T_{LM}}\right]^{\frac{1}{4}} \quad \text{(Equation 3)}$$

where g, ρ_l, ρ_v, k_l, λ_{fg}, and μ_l represent the acceleration of gravity, liquid density, vapor density, thermal conductivity, latent heat of vaporization, and viscosity of water. The liquid and vapor properties correspond to the saturation temperature.

Table 2. Parametric study cases

Series	Texturing	Functionalization	Infused lubricant
1	Vary	Fixed – mercaptan	Fixed – Krytox 104
2	Fixed – Etched	Vary	Fixed – Krytox 104
3	Fixed – Etched	Fixed – mercaptan	Vary

Heat transfer performance

In the first parametric test series, test sections were fabricated using five different surface texturing methods—etched, 0.5 V electrodeposited, 0.6 V electrodeposited, 0.7 V electrodeposited, and 1.1 V electrodeposited. The test sections were all functionalized with mercaptan and infused with Krytox 104. The results of heat transfer experiments for the various textures are plotted as a function of mean peak spacing (s) in Figure 4 with best-fit power function curves through the data. Variations in h_c and ε did not show correlation with the peak-to-valley asperity height (a). For a fixed ΔT_{LM}, h_c and ε increase proportionally with s. As expected, the condensation heat transfer coefficient in Figure 4A shows an inverse dependence with ΔT_{LM}, similar to the Nusselt correlation (Equation 3). At high ΔT_{LM} of 20°C, h_c increases by 60% from approximately 25 kW/m^2-°C to 40 kW/m^2-°C as s triples from 60 μm to 186 μm. Likewise, ε increases from 0.84 to 0.91 over the same range, indicating that the overall effectiveness of the heat transfer system improved by only 7 percentage points despite a 60% increase in h_c. The range of measured condensation heat transfer coefficient and its trend with the logarithmic mean temperature difference match those reported for DWC in pure steam by Baojin et al. (2011), Chung et al. (2004), Kim et al. (2019) and Zhang et al. (2020).

In the second parametric test series, test sections were fabricated using five different functionalizing agents: mercaptan, stearic acid, octylphosphonic acid, silane, and Sylgard-184 along with an unfunctionalized test section. All the test sections were etched prior to functionalization to give them the same texturing and, following functionalization, they were all infused with Krytox 104. The results of heat transfer experiments for varied functionalizing agents are shown in Figure 5A for heat transfer coefficient and in Figure 5B for the heat transfer effectiveness both in terms of the logarithmic mean temperature difference. Mercaptan produced the best heat transfer results followed closely by stearic acid, both agents achieving h_c values 4–7 times greater than the Nusselt correlation and ε values at or above 0.88 across the entire ΔT_{LM} range. Functionalization with octylphosphonic acid produced h_c values roughly twice as much as the Nusselt correlation and ε values in the range 0.79–0.85. The silane and Sylgard-184 functionalized test sections produced h_c approximately 1–1.5 times greater than the Nusselt correlation and ε values in the range 0.70–0.82. The unfunctionalized test section in which Krytox 104 was applied directly to the etched surface significantly underperformed not only the functionalized test sections but also the Nusselt correlation prediction. This series of tests effectively demonstrated two important characteristics of LIS. First, direct application of lubricant to a roughened surface does not improve its heat transfer performance. Indeed, the lubricant inhibits heat transfer due to added thermal resistance, as would be expected of any coating on a condensing surface. The surface must be functionalized with an agent that lowers the surface energy of the substrate prior to lubricant infusion. Second, different functionalizing agents perform differently on the condensing surface, with mercaptan performing best of the agents evaluated in this series of tests.

In the third parametric test series, test sections were fabricated using six different lubricant viscosities. All test sections were etched and functionalized with mercaptan, then infused with one of the Krytox lubricants. Krytox 101–105 vary in viscosity (μ) from 14.7 mPa-s to 310.4 mPa-s (Table S2). Additionally, a sixth infusion lubricant was created from 50% mixtures (by volume) of Krytox 103 and Krytox 104 to obtain a lubricant with μ of 86.7 mPa-s. The results of heat transfer experiments for varied μ are shown in Figure 6. Both h_c (Figure 6A) and ε (Figure 6B) show a trend across the ΔT_{LM} range, increasing with μ until the 50-70 mPa-s range, and then decreasing again with increasing μ. The low heat transfer performance at the lowest lubricant viscosity is likely due to the faster drainage of lubricant due to condensate shear via cloaking and gravity. The depletion of lubricant layer opens the possibility of steam exposure to underlying rough surfaces that can cause condensate pinning and increase the thermodynamic barrier to nucleation. Higher viscosity lubricants are more stable due to less drainage; however, the sliding ability or mobility of the condensate droplet is compromised by the higher viscosity, limiting the condensation heat transfer increase. This

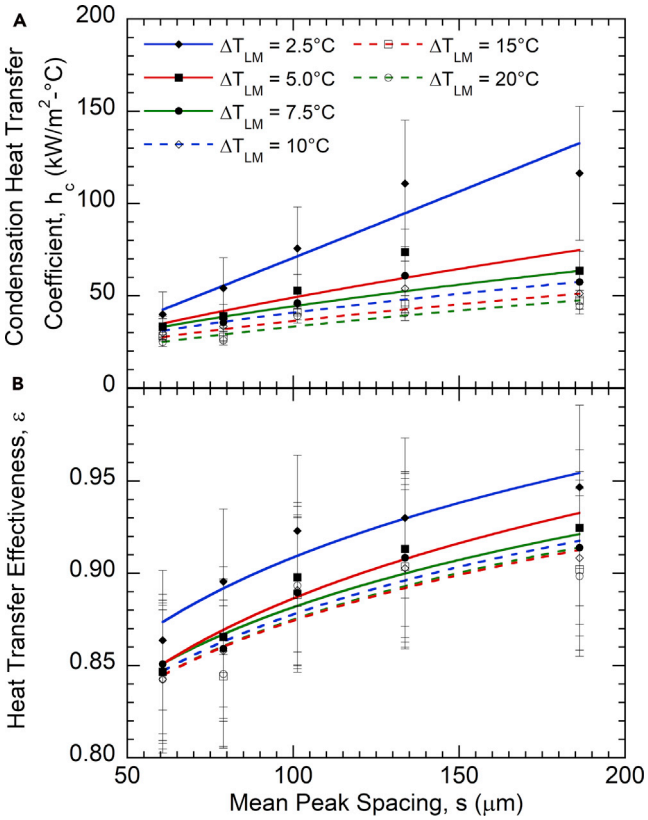

Figure 4. Heat transfer performance of LIS as a function of surface texture

(A) Condensation heat transfer coefficient and (B) Heat transfer effectiveness as a function of mean peak spacing for different texturing, functionalized with mercaptan and infused with Krytox 104. Data are represented as mean ±95% CI.

tradeoff is the basis for optimal lubricant viscosity for maximum h_c and ε observed in Figure 6. Further, the maximum values for h_c and ε occur near 50-70 mPa-s, which correspond closely to the viscosities of Krytox 103 and the Krytox 103/104 mixture.

Retained lubricant

Retention of infused lubricant through a heat transfer test is a key indicator of durability. From warm-up through data collection, each test section was subjected to test conditions for approximately one hour. During testing, a test section was weighed before lubricant infusion and after condensation heat transfer testing. The test section pre-infusion weight was subtracted from the post-test weight to find retained lubricant mass, which was converted to retained volume (V_L^1) using lubricant density. Additionally, the maximum possible lubricant volume, V_L^0, was determined for each texturing method using parameters *a* and *s* in Table 1 and estimating volume of the asperities by characterizing them as triangular cavities formed around the circumference of the tube. Calculated values of V_L^0 are included in Table 1.

Retained lubricant volume (V_L^1) data for each of the parametric studies are summarized in Figure 7. Figures 7A–7C, respectively, show the effect of texturing, functionalizing agent, and infused lubricant on V_L^1. Texturing had a significant effect on V_L^1 with the highest retention of 89.5 μL occurring on the 0.7 V electrodeposited test section and the lowest retention of 1.7 μL occurring on the 0.5 V electrodeposited test section. The correlation between lubricant retention and texturing was significant enough to warrant further examination, which will be discussed below. Effect of functionalizing agent on V_L^1 of etched test sections (Figure 7B) was minimal, with the unfunctionalized test section retaining 3.7 μL and the silane functionalized test section retaining 2.6 μL as the best and worst cases, respectively. This result shows no correlation with heat transfer performance results presented in Figure 5, suggesting that functionalizing agent can be selected for heat transfer performance without suffering a lubricant retention penalty. Lubricant viscosity

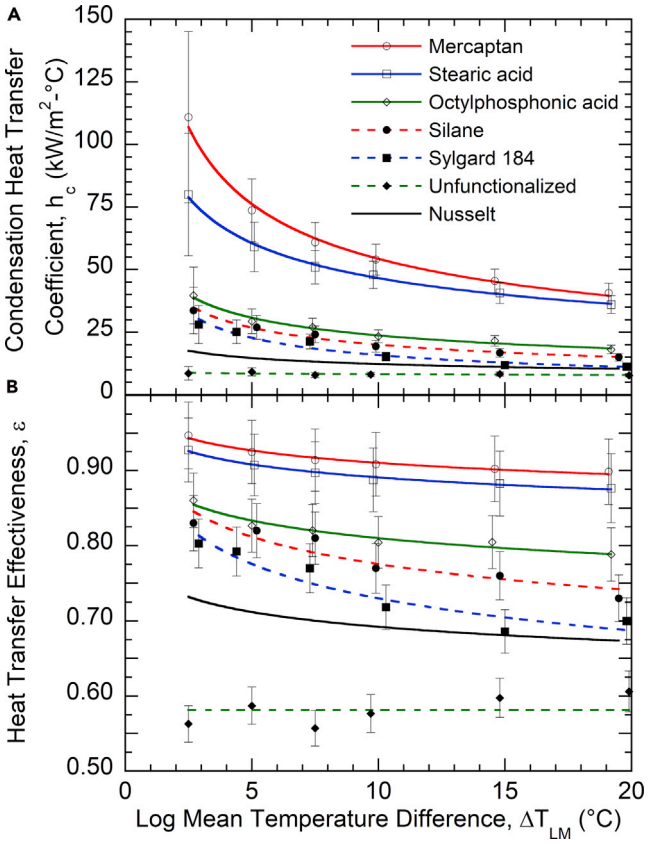

Figure 5. Heat transfer performance of LIS for various functionalizing agents

(A) Heat transfer coefficient and (B) Heat transfer effectiveness as a function of logarithmic mean temperature difference for etched test sections, functionalized with various agents, and infused with Krytox 104. Data are represented as mean ±95% CI.

had a moderate effect on V_L^1 (Figure 7C), with retention volume increasing with lubricant viscosity. The etched test section infused with low viscosity Krytox 101 retained 1.9 μL, while the test section infused with high viscosity Krytox 105 retained 3.9 μL. This result is expected since higher viscosity decreased the lubricant's susceptibility to removal by shear.

For a systematic comparison of texturing effect observed in Figure 7A, lubricant retention was expressed as a fractional retention (v_L^R) of maximum possible lubricant volume (V_L^0) using the relationship $v_L^R = V_L^1 / V_L^0$. Retained lubricant fraction may be understood to be a balance between the forces during condensation that seek to remove the lubricant from the asperity valleys and the adhesive capillary force that keeps the lubricant in the asperity valleys. In the model of the asperity valleys sketched in the inset in Figure 8, v_L^R is not dependent on the asperity height, *a*, but instead depends on the mean peak spacing, *s*, as presented in Figure 8. As expected, the retained volume fraction decreases with increasing asperity width from about 0.95 to 0.10, and this variation is seen to be as s^{-2}. The narrow, deep asperities correspond to smaller *s* values and the wide shallow asperities correspond to larger *s* values. A smaller *s* value results in higher adhesion force due to capillary action between lubricant and the textured surfaces which increased lubricant retention.

Taguchi robust parameter analysis

Figures 4, 5, 6, 7, and 8 present the effect of one design parameter at a time on the condensation heat transfer and durability performances of LISs. It is of further interest to understand possible interactions among the three design components of texturing, functionalizing agent, and infused lubricant achieved by various combinations of parameters.

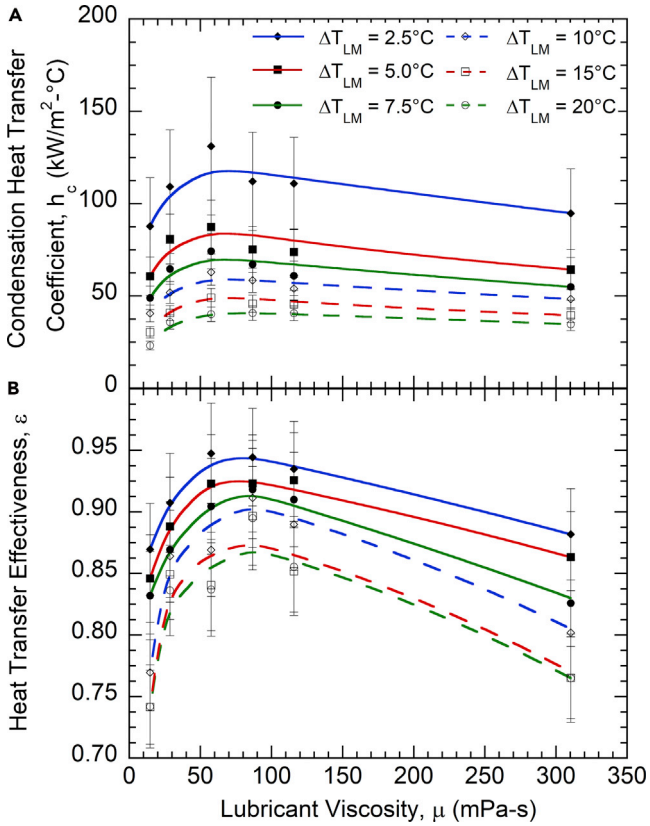

Figure 6. Heat transfer performance of LIS as a function of lubricant viscosity

(A) Heat transfer coefficient and (B) Heat transfer effectiveness as a function of lubricant viscosity for etched test sections, functionalized with mercaptan, and infused with Krytox lubricants of differing viscosities. Data are represented as mean ±95% CI.

The performance results from the parametric study showed that 0.7 V electrodeposited texturing with the smallest mean peak spacing value (Table 1) resulted in the lowest heat transfer performance (Figure 4). Among the lubricant choices, Krytox 101 was the least viscous and displayed the lowest heat transfer performance (Figure 6) and least lubricant durability in terms of v_L^R (Figure 7C). Functionalizing agents showed minimal impact on v_L^R (Figure 7B) but had a significant impact on the heat transfer performance (Figure 5). Mercaptan and stearic acid ranked first and second in heat transfer performance, while the unfunctionalized test section ranked worst. These three choices provided a large range of heat transfer performance characteristics while preserving the unfunctionalized case as a baseline. Further, since octylphosphonic acid, silane and Sylgard-184 showed similar heat transfer performance and lubricant retention attributes (Figures 5 and 7), Sylgard-184 was chosen for further study due to its substrate adhering mechanism. While mercaptan, stearic acid, octylphosphonic acid, and silane all adhere to the substrate via adsorption, Sylgard-184—an elastomer—cures to the substrate during the functionalization process. In comparison to the other functionalizing agents, this property of Sylgard-184 makes it perhaps the most universally applicable functionalizing agent for substrates other than copper. Hence, the above four design options—0.7 V electrodeposited texturing, Krytox 101 infused lubricant, and octylphoshphonic acid and silane functionalizing agents—were eliminated from the design of experiments matrix.

Since full factorial analysis of the remaining four texturing methods, four functionalizing agents, and four lubricant viscosities would require 64 experiments, a Taguchi L-16 orthogonal array (Phadke, 1989) experimental design model was instead chosen to examine the three design factor and four design level parameter interactions. Two objective functions were targeted in the Taguchi analysis— $-\ -\ -\varepsilon$ and v_L^R—with the goal of finding optimal combinations of texturing, functionalizing agent, and lubricant viscosity design parameters across the ΔT_{LM} range of 2.5°C–20°C. As compared with the previously explained parametric studies that analyzed a single design parameter at a time, the Taguchi orthogonal array allowed for interactions between the design parameters to

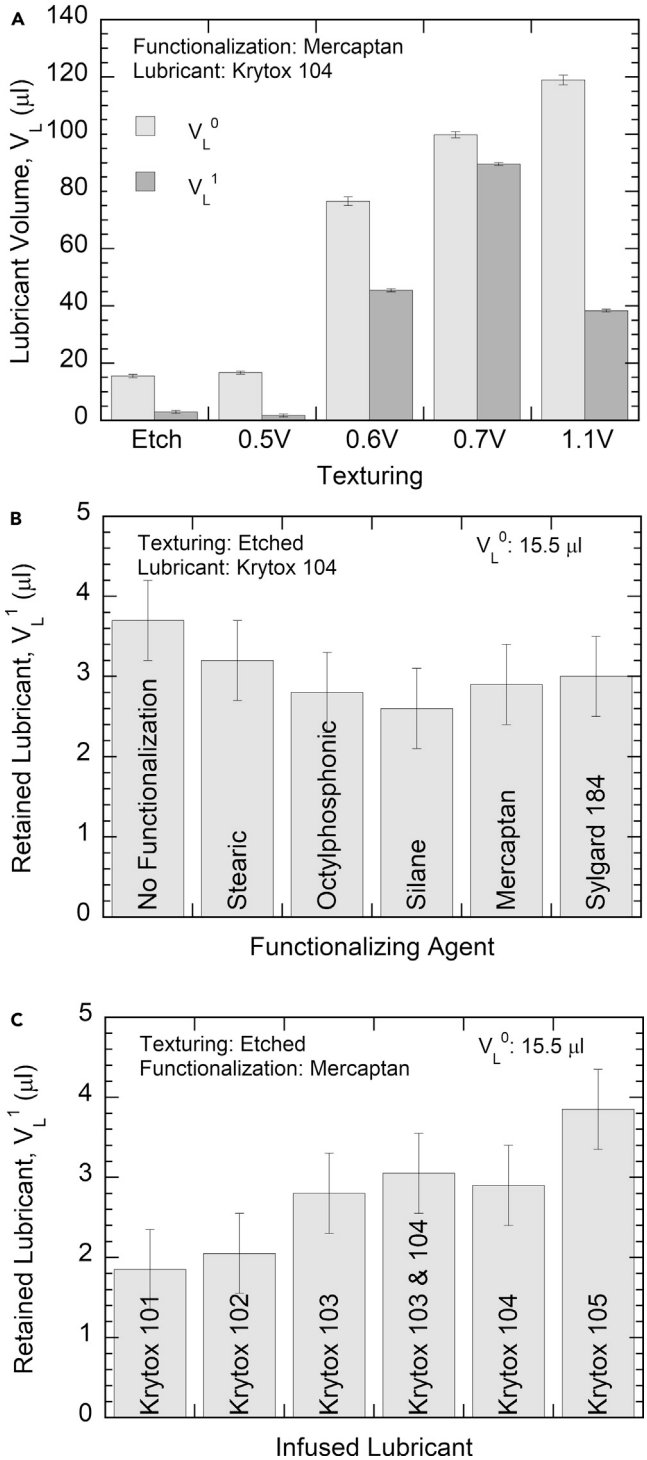

Figure 7. Post-test retained lubricant on LIS

Retained lubricant volume on test sections with (A) varying substrate texturing; (B) varying functionalizing agents; and (C) varying infused lubricants. Data are represented as measurement ± instrument resolution uncertainty.

manifest. Table 3 shows the L-16 orthogonal array used for analysis. All 16 test section configurations were evaluated in the test apparatus described in transparent methods (supplemental information; Figure S1; Table S1). After performing all experiments, an analysis of means was used to estimate factor effects on ε and v_L^R.

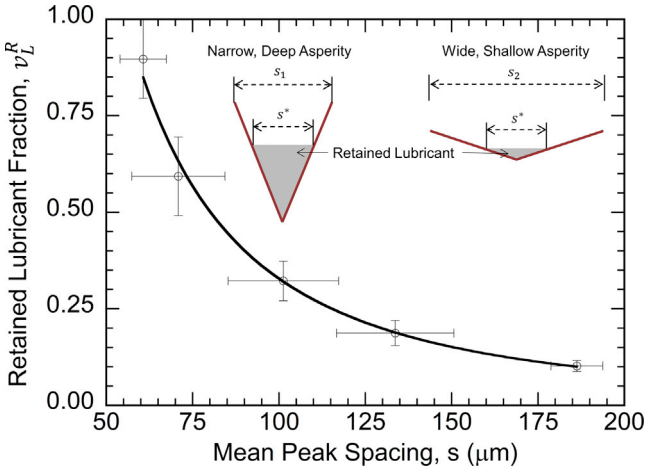

Figure 8. Retained lubricant volume fraction as a function of mean peak spacing on test sections functionalized with mercaptan and infused with Krytox 104

Inset: Simplified diagrams of a narrow, deep asperity and a wide, shallow asperity showing lubricant retention. Data are represented as mean ± SD.

Figures 9A and 9B present an analysis of means on the heat transfer effectiveness ε and the retained lubricant volume fraction, respectively. It is seen from Figure 9A that ε was moderately sensitive to texturing as represented by *s*, highly sensitive to functionalizing agent, and minimally sensitive to lubricant viscosity (μ). As in the parametric analysis, heat transfer performance varied almost linearly with *s*, showing an *s*-dependent mean spread for ε between 0.74 and 0.86 as compared to the overall mean of 0.80. Functionalization, however, showed a clear breakout of both mercaptan and stearic acid (functionalizing agents 1 and 2 in Figure 9A) for achieving high heat transfer effectiveness compared to Sylgard-184 and the unfunctionalized case (functionalizing agents 3 and 4). As with the earlier parametric study on etched tubes, mercaptan slightly outperformed stearic acid. The Taguchi analysis result, however, shows that this trend holds across all texturing methods and lubricant viscosities tested. The functionalizing agent showed mean spread in the values of effectiveness between 0.90 and 0.64 with the lowest value obtained for unfunctionalized surface. Heat transfer performance was minimally dependent on μ, showing a viscosity-dependent mean spread of only 0.07, which indicates 4-times less sensitivity of heat transfer effectiveness to μ than to functionalizing agent. These results reinforce the findings of the parametric study across a wider variety of design parameters.

From Figure 9B, it is evident that lubricant retention volume fraction (v_L^R) was highly sensitive to *s*, minimally sensitive to functionalizing agent, and moderately sensitive to μ. Qualitatively, this result matches the parametric analysis. Quantitatively, the spread between the highest retention mean for *s* of 79.0 μm and the lowest retention mean for *s* of 186.3 μm was 0.48, representing a factor of 1.5-times the mean retention for all 16 experiments of 0.31. This demonstrates strong, inverse correlation between *s* and v_L^R. Lubricant retention for texturing with low *s* value is higher because the capillary force that holds the lubricant in place scales inversely with mean peak spacing between asperities. The mean spread for both functionalization agent and lubricant viscosity were 0.10 and 0.21, respectively, indicating that oil retention is up to 5-times less sensitive to these factors than to *s*. As expected, the high viscosity lubricant showed better retention due to low-susceptibility to depletion via droplet shear.

Examining both ε and v_L^R together from the Taguchi mean plots reveals clear trends. First, both ε and v_L^R showed minimal sensitivity to μ over the range tested. The slight trend, however, was that lubricant viscosity of 57.6 mPa-s contributed to higher heat transfer performance (Figure 9A) and higher viscosity contributed to higher lubricant retention (Figure 9B). This trend is similar to the results obtained from the parametric study presented earlier, where ε appeared to peak at viscosities between 50 and 70 mPa-s (Figure 6). Second, functionalizing agent had a significant impact on ε and a minimal impact on v_L^R. This result reinforces the parametric study and demonstrates that durability of the LIS due to shedding is minimally dependent on the functionalizing agent chosen, allowing for maximization of heat transfer performance without a

Table 3. Taguchi L-16 orthogonal array

Run	Texturing	s (μm)	Functionalizing Agent (level)		Lubricant	μ (mPa s)
1	Etched	133.7	Mercaptan	(1)	Krytox 102	28.7
2	Etched	133.7	Stearic acid	(2)	Krytox 103	57.6
3	Etched	133.7	Sylgard-184	(3)	Krytox 104	115.8
4	Etched	133.7	None	(4)	Krytox 105	310.4
5	0.6V Electrodeposited	79.0	Mercaptan	(1)	Krytox 103	57.6
6	0.6V Electrodeposited	79.0	Stearic acid	(2)	Krytox 102	28.7
7	0.6V Electrodeposited	79.0	Sylgard-184	(3)	Krytox 105	310.4
8	0.6V Electrodeposited	79.0	None	(4)	Krytox 104	115.8
9	0.5V Electrodeposited	186.3	Mercaptan	(1)	Krytox 104	115.8
10	0.5V Electrodeposited	186.3	Stearic acid	(2)	Krytox 105	310.4
11	0.5V Electrodeposited	186.3	Sylgard-184	(3)	Krytox 102	28.7
12	0.5V Electrodeposited	186.3	None	(4)	Krytox 103	57.6
13	1.1V Electrodeposited	101.3	Mercaptan	(1)	Krytox 105	310.4
14	1.1V Electrodeposited	101.3	Stearic acid	(2)	Krytox 104	115.8
15	1.1V Electrodeposited	101.3	Sylgard-184	(3)	Krytox 103	57.6
16	1.1V Electrodeposited	101.3	None	(4)	Krytox 102	28.7

durability penalty. Third, ε and v_L^R are oppositely correlated with s, indicating a fundamental link between heat transfer performance and lubricant retention that will be further examined.

Figure 10 shows the qualitative difference between a test section with strong heat transfer performance and one with poor performance. Figure 10A is a photograph of sustained DWC on a test section with 0.5 V electrodeposited texturing, functionalized with mercaptan, and infused with Krytox 104. The largest droplet size observed is approximately 2.7 mm in diameter, which is the capillary length (l_c) of water at 40°C calculated from $l_c = \sqrt{\sigma/\rho g}$ where σ is the surface tension of water, ρ is its density, and g is the acceleration due to gravity. This ensures that gravity complements droplet shedding from the condensing tube surface and refreshes it for continuous nucleation. This test section achieved h_c and ε values of 116.4 kW/m^2-°C and 0.949, respectively, at ΔT_{LM} of 2.5°C. Conversely, Figure 10B shows clear FWC on a test section with 1.1 V electrodeposited texturing, no functionalization, and infused with Krytox 102. Despite having a lower viscosity lubricant on the surface, the lack of a functionalizing agent led to sustained FWC. The measured values for h_c and ε are 6.2 kW/m^2-°C and 0.488, respectively, at ΔT_{LM} of 2.5°C.

Heat transfer performance and retained lubricant interaction

Lubricant infusion on condensing surfaces leads to two contrasting effects on heat transfer performance improvement. First, it promotes DWC, leading to rapid droplet shedding (Videos S1–S5) and enhanced heat transfer effectiveness as compared to FWC (Video S6). Second, due to its low thermal conductivity in comparison to metal, infused lubricant serves as an insulating barrier to heat transfer over any portion of the surface covered. As observed in the parametric study and Taguchi analysis, changes in mean peak spacing (s) create trade-offs in ε and v_L^R. This tradeoff occurs because heat transfer performance and lubricant retention are directly related by surface geometry and in particular, asperity geometry. The inset of Figure 8 shows simplified diagrams of a narrow, deep asperity and a wide, shallow asperity. From the measurement of post-test lubricant volume and considering the topographical features of the asperities characterized by mean peak spacing (s) and peak-to-valley height (a) for calculation of post-test lubricant fill level, it was determined that there is a critical asperity spacing (s^*) where lubricant shedding stops, indicating that v_L^R is a function of asperity geometry and not a function of time.

The critical asperity spacing, s^*, results in two advantages on the wide, shallow asperity. First, more surface area is available for condensation as a larger area of the wide, shallow asperity is not covered by lubricant. Second, the thickness of the remaining volume fraction of lubricant on the wide, shallow asperity is less than that remaining on the narrow asperity, reducing the insulating effect of the lubricant on the surface. Both

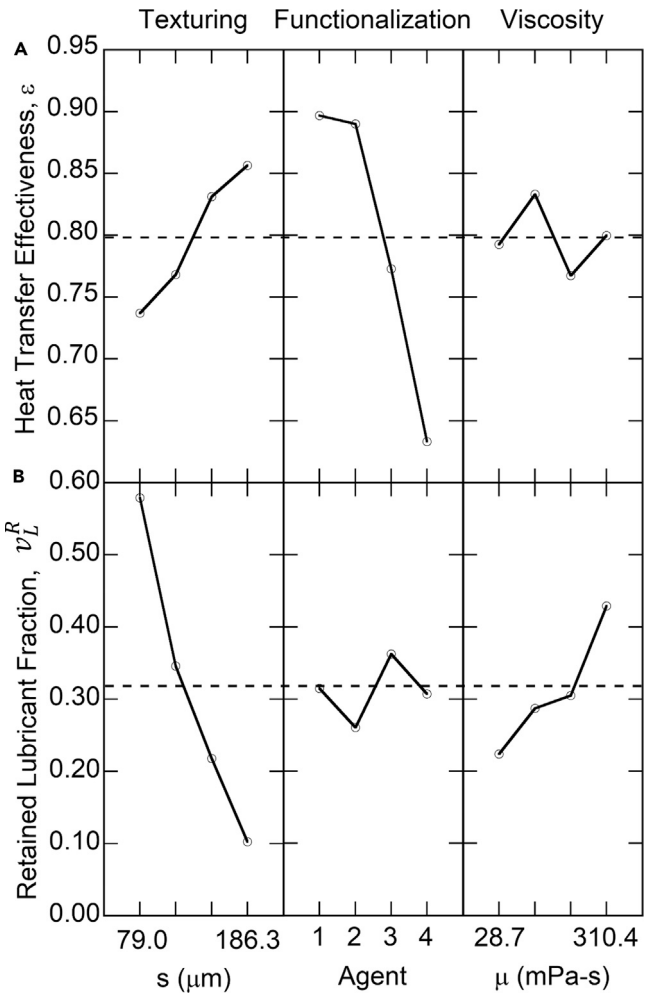

Figure 9. Taguchi analysis of means plots

Taguchi analysis of means plots for (A) heat transfer effectiveness and (B) lubricant retention volume fraction as a function of texturing, functionalizing agent, and lubricant viscosity.

factors lead to better heat transfer performance of the wide, shallow asperity and demonstrate the dependence of ε on v_L^R and the dependence of v_L^R on surface geometry. The observed experimental behavior also shows that narrow asperities represented by smaller s values retain a higher volume fraction of oil (Figure 8) than wide asperities with correspondingly lower heat transfer performance (Figure 4). A hybrid, solid-lubricant surface experiences trade-offs between increased thermal resistance due to retained lubricant and increased droplet mobility and shedding due to retained lubricant. For this reason, both lubricant retention limits$---v_L^R$ of 1 or 0—are undesirable. Based on the foregoing considerations, in this study, a clear correlation is derived for both v_L^R and ε that is dependent on properties of the lubricants, working fluid and working temperatures of the condensing surface.

Experimental analysis shows that two factors are dominant for v_L^R: capillary forces and viscous forces. The dimensionless Bond number relates gravitational force to surface tension force and is often used to describe processes where capillary forces are dominant (Incropera et al., 2007). The Bond number is defined as:

$$Bo = \frac{\Delta\rho g l^2}{\sigma} \qquad \text{(Equation 4)}$$

where $\Delta\rho$ is the difference in density between two fluids in contact (lubricant and steam, in the present case), g is the acceleration of gravity, σ is surface tension, and l is a characteristic length. Additionally, a

viscosity ratio can be defined for the two fluids in contact as μ_w/μ_L where μ_L is lubricant viscosity and μ_w is the viscosity of the condensed fluid (liquid water in this study).

The experimentally measured values of retained lubricant fraction, v_L^R, for all the cases in the parametric studies and the Taguchi analysis are plotted in Figure 11A in terms of a modified Bond number, Bo', defined by using s for the characteristic length, l, in Equation 4 and multiplying by viscosity ratio to the 1/3-power as:

$$Bo' = \frac{(\rho_L - \rho_v) g s^2}{\sigma_L} \left(\frac{\mu_w}{\mu_L}\right)^{1/3} \quad \text{(Equation 5)}$$

where ρ_L is lubricant density and ρ_v is density of steam at saturation conditions ($T_v = 40°C$). It is seen that the data are represented on this plot in a unified manner, bringing together the effects of all the governing parameters. The plot reveals that the retained lubricant fraction data follow a consistent trend with respect to $1/Bo'$ that may be expressed concisely as:

$$v_L^R = \tanh\left(\frac{1}{1117\ Bo'}\right) \quad \text{(Equation 6)}$$

which is shown as the solid curve in Figure 11A. The dashed lines represent the $\pm 10\%$ error bands about the correlation, and demonstrate that all the measured data fall inside the dashed lines to within the experimental measurement errors, representing a remarkable level of accuracy. Although the data in the plot are for $75 \leq 1/Bo' \leq 1900$, the correlation in Equation 6 obeys physical consistency checks as follows: v_L^R increases asymptotically toward 1.0 as $1/Bo' \rightarrow \infty$ (small ρ_L, s, or μ_w or large surface tension, σ_L or lubricant viscosity, μ_L) and $v_L^R \rightarrow 0$ as $1/Bo' \rightarrow 0$ (large ρ_L, s, or μ_w or small surface tension, σ_L or lubricant viscosity, μ_L). Equation 6 represents the first ever model for relating the retained lubricant fraction in LISs to the governing physical and geometrical parameters in a unified manner, expressed in terms of a dimensionless parameter.

Both the parametric study and the Taguchi analysis showed that ε is highly dependent on the functionalizing agent applied underneath the infused lubricant. Further, the Taguchi analysis demonstrated that the functionalizing agent had little impact on v_L^R, while mercaptan maximized ε. Accordingly, the data on the heat transfer effectiveness for the case of mercaptan is further examined here. Figure 11B shows all heat transfer effectiveness data from the mercaptan-functionalized test sections in this study, that can be effectively represented by the following analytical equation:

$$\varepsilon = \left[1 + 0.036\left(\frac{\theta'}{Bo'}\right)^{1/4}\right]^{-1} \quad \text{(Equation 7)}$$

where θ' is a dimensionless logarithmic mean temperature difference, $\theta' = (\Delta T_{LM}/T_v)^{3/4}$. Note that ε is dependent on both logarithmic mean temperature difference and the governing physical and geometry parameters controlling v_L^R, that are concisely encapsulated by the dimensionless groups in Equation 7. Equation 7 is graphically represented by the solid line in Figure 11B while the dashed lines represent the ± 0.025 interval about the correlation. It is seen that the correlation unifies the data for all the mercaptan-functionalized texturing methods, lubricants, and logarithmic mean temperature differences studied, and the data falling entirely within the ± 0.025 error band represents excellent accuracy of the prediction. Equation 7 is derived based on data in the range $75 \leq 1/Bo' \leq 1900$ and $0.125 \leq \theta' \leq 0.6$, which represent the ranges of its validity.

Equations 5, 6, and 7, and Figure 11 together show four fundamental findings. First, v_L^R is directly proportional to the properties of the infused lubricant and the working fluid, as given by Equations 5 and 6. Second, ε and v_L^R are related through the surface geometry of the asperities, which control the distribution of the retained lubricant as demonstrated in Figure 11. Third, as evident in Equation 7, ε is proportional to lubricant properties, condensing fluid properties, asperity geometry, and operating ΔT_{LM} of the condensing surface. Finally, the heat transfer enhancements due to DWC promotion through enhanced droplet mobility on LIS far outweigh the increased thermal resistance from the infused low thermal conductivity lubricant.

Figure 11, Equations 6, and 7 demonstrate mathematically the observed experimental trade-offs between heat transfer improvements in terms of the effectiveness, ε, and LIS durability quantified in terms of v_L^R. While the infused lubricant acts as an insulating layer to a small extent, the improved heat transfer due to sustained DWC significantly overcomes this small insulating effect. Additionally, v_L^R of either 0 or 1 is not desirable

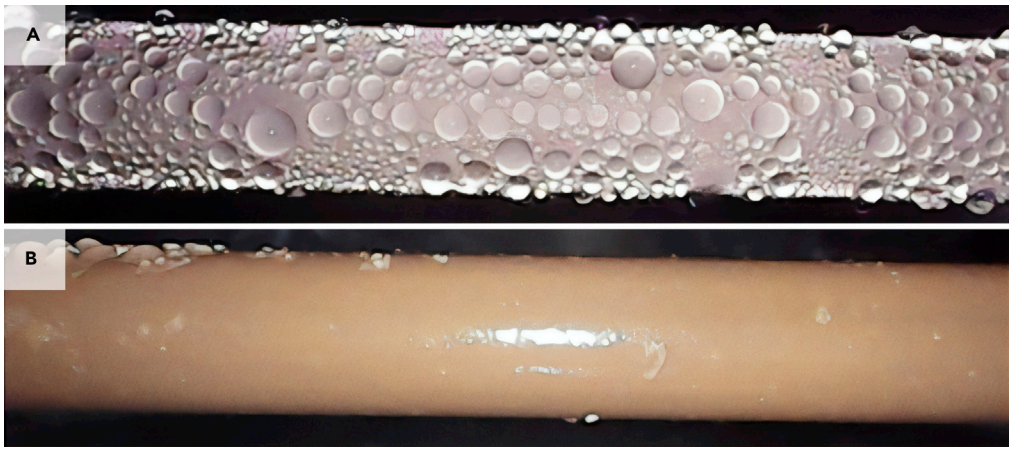

Figure 10. Images of sustained DWC and FWC on test sections

Images of (A) test section with 0.5V electrodeposited texturing, mercaptan functionalization, and Krytox 104 lubricant infusion showing continuous DWC; (B) test section with 1.1V electrodeposited texturing, no functionalization, and Krytox 102 lubricant infusion showing FWC. Videos S1, S2, S3, S4, and S5 show DWC on LIS. Video S6 shows FWC on a surface without lubricant infusion.

since the first case would not promote DWC and the second case would cover the majority of heat transfer surface with lubricant leading to high thermal resistance. In view of these considerations, Equations 6 and 7 may be used to predict the potential heat transfer performance of any lubricant-infused surface design and conversely, may be used to design the lubricant-infused surfaces for a desired target condensation heat transfer performance. As an example of the former, for a lubricant-infused surface with $1/Bo' = 75$ Equation 6 provides a retained lubricant volume fraction of $v_L^R = 0.067$, and the corresponding heat transfer effectiveness is obtained from Equation 7 as $\varepsilon = 0.94$ at $\Delta T_{LM} = 2.5°C$ and $\varepsilon = 0.92$ at $\Delta T_{LM} = 20°C$. For comparison, the effectiveness for FWC ranges from 0.74 at $\Delta T_{LM} = 2.5°C$ to 0.63 at $\Delta T_{LM} = 20°C$. Therefore, the use of LIS results in an increase in heat transfer effectiveness by 27% and 46% at $\Delta T_{LM} = 2.5°C$ and 20°C, respectively, relative to an FWC surface. Finally, Equations 6 and 7 and the use of the heat transfer effectiveness as a performance parameter may also serve to unify the data reported on the various configurations in the literature. The use of heat transfer effectiveness as a performance parameter allows for a holistic understanding of system improvements stemming from the increased surface condensation heat transfer. We propose heat transfer effectiveness as a standard parameter to be adopted for reporting data in the field in the future.

Conclusions

The study presented two facile fabrication methods for creating multiscale texturing on copper tubes that were used to systematically study functionalization using a series of non-wetting agents and infusion using various viscosities of lubricants. The effect of each step of the fabrication process on heat transfer performance and lubricant retention of the surface was systematically examined to quantify the trade-offs between heat transfer improvements and surface durability in conditions representative of actual water-cooled power plant condensers. Surface texturing, as quantified by mean peak spacing, showed direct relationship with heat transfer performance and inverse relationship with lubricant retention. Six different functionalized conditions were tested, showing no lubricant retention dependence on functionalizing agent. Heat transfer performance, however, was strongly dependent on functionalizing agent with mercaptan showing the strongest performance in parametric studies and in a Taguchi experimental matrix. Lubricant retention showed a slight, direct dependence on viscosity, while heat transfer performance demonstrated a slight, inverse correlation to viscosity.

Heat transfer performance data were presented in terms of both condensation heat transfer coefficient and heat transfer effectiveness. The use of heat transfer effectiveness was shown to provide a holistic understanding of system improvements realized by the enhanced heat transfer on the condensing surface. The results show that the least amount of lubricant that maintains dropwise condensation is sufficient to achieve maximum heat transfer effectiveness. Finally, from the experimental studies a pair of analytical expressions was developed that relate the heat transfer effectiveness and the retained lubricant volume fraction of mercaptan-functionalized surfaces to the governing physical and geometrical parameters in unified manner

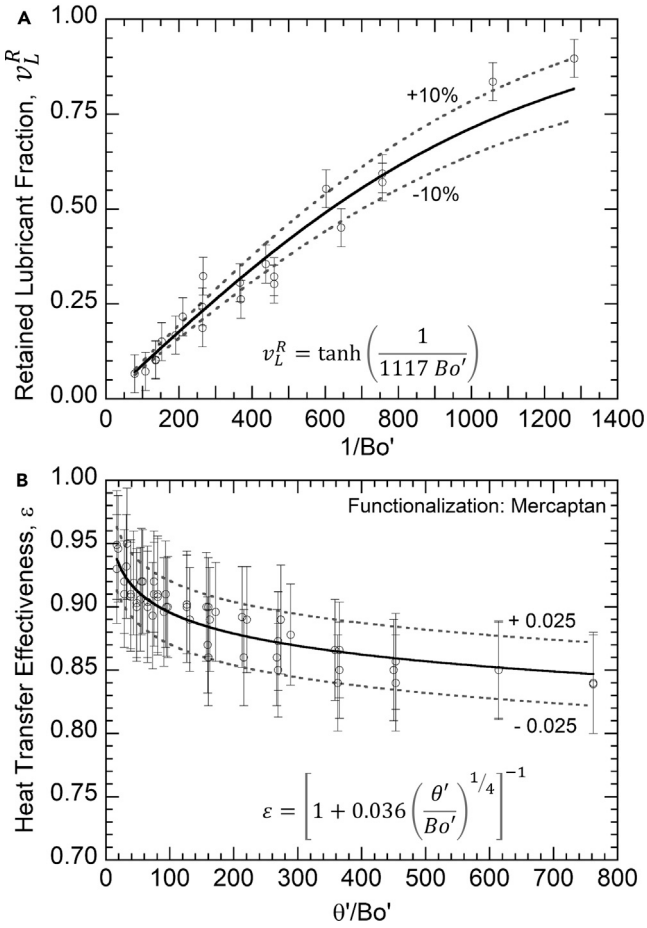

Figure 11. Analytical relationships for retained lubricant volume fraction and heat transfer effectiveness

Correlation of (A) retained lubricant volume fraction with the inverse of the modified Bond number and (B) heat transfer effectiveness with θ'/Bo'. Data are represented as mean ±95% CI.

through a Bond number, a viscosity ratio and a dimensionless logarithmic mean temperature difference. These correlations allow *a priori* design prediction of LISs for practical use in condenser applications. The results clearly demonstrate the merit to adopt heat transfer effectiveness as a standard parameter for quantifying the significance of condensation heat transfer enhancement on system performance that is of immense value from an applied perspective.

Limitations of the study

The study presented heat transfer effectiveness as a more appropriate way of analyzing the enhancement in condensation heat transfer achieved through the use of LISs. It must be mentioned that although the effectiveness at a given h_c value is slightly higher for lower thermal conductivity tube material (Figure 3A), the resulting heat rate will be lower because the maximum achievable heat rate decreases with increase in thermal resistance from the tube wall material (Equation 1). A higher effectiveness only implies that the condenser system is closer to reaching its maximum achievable heat rate. Although the range of measured condensation heat transfer coefficient and its trend with the logarithmic mean temperature difference in this study match those reported in the literature well, specific comparison to individual literature values requires information on the asperity structural parameters of the surfaces used, which are not available comprehensively in the literature studies. Future studies are encouraged to use the approach of reporting effectiveness values and in terms of the non-dimensional relationships presented in this article.

Resource availability

Lead contact

Further information requests should be directed to the lead contact, Professor Ranga Pitchumani (pitchu@vt.edu).

Materials availability

Materials used in the study are commercially available.

Data and code availability

All data and analytical methods are reported in the main text or in the supplemental information section.

METHODS

All methods can be found in the accompanying Transparent methods supplemental file.

SUPPLEMENTAL INFORMATION

Supplemental information can be found online at https://doi.org/10.1016/j.isci.2021.102336.

ACKNOWLEDGMENTS

The material reported in this publication is based upon work supported by the U.S. Department of Energy under Award Number DE-FE0031556.

AUTHOR CONTRIBUTIONS

R.S. and R.P. designed the study; R.S. conducted the experiments; R.S., K.N., and R.P. analyzed the data, wrote and edited the paper; R.P. was the principal investigator and supervised the work.

DECLARATION OF INTERESTS

The authors declare no competing interests.

Received: January 20, 2021
Revised: March 7, 2021
Accepted: March 16, 2021
Published: April 23, 2021

REFERENCES

Anand, S., Paxson, A.T., Dhiman, R., Smith, J.D., and Varanasi, K.K. (2012). Enhanced condensation on lubricant-impregnated nanotextured surfaces. ACS Nano *6*, 10122–10129.

Attinger, D., Frankiewicz, C., Betz, A.R., Schutzius, T.M., Ganguly, R., Das, A., Kim, C.-J., and Megaridis, C.M. (2014). Surface engineering for phase change heat transfer: a review. MRS Energy Sustain. *1*, 1–40.

Bao, J., Lin, Y., Zhang, R., Zhang, N., and He, G. (2017). Strengthening power generation efficiency utilizing liquefied natural gas cold energy by a novel two-stage condensation Rankine cycle (TCRC) system. Energy Convers. Manag. *143*, 312–325.

Baojin, Q., Li, Z., Hong, X., and Yan, S. (2011). Experimental study on condensation heat transfer of steam on vertical titanium plates with different surface energies. Exp. Therm. Fluid Sci. *35*, 211–218.

Bilgil, A., and Hırlakoğlu, B. (2017). An experimental study on desalination at vacuum environment under low pressure and low condensation temperatures. Desalination *411*, 9–18.

Brenner, L., Tillenkamp, F., Krütli, M., and Ghiaus, C. (2020). Optimization potential index (OPI): an evaluation method for performance assessment and optimization potential of chillers in HVAC plants. Appl. Energy *259*, 114111.

Cao, F., Liu, Q., and Xiao, H. (2020). Experimental study of a humidification-dehumidification seawater desalination system combined with the chimney. Int. J. Photoenergy *2020*, 1–9.

Chuang, C.C., and Sue, D.C. (2005). Performance effects of combined cycle power plant with variable condenser pressure and loading. Energy *30*, 1793–1801.

Chung, B.J., Kim, S., and Kim, M.C. (2004). Experimental comparison of film-wise and drop-wise condensations of steam on vertical flat plates with the presence of air. Int. Commun. Heat Mass Transf. *31*, 1067–1074.

Fakheri, A. (2007). Heat exchanger efficiency. J. Heat Transfer *129*, 1268–1276.

Guyer, J.P. (2013). An introduction to condensers and auxiliary equipment for steam power plants, Continuing Education and Development Course No.: D03-003, Continuing Education and Development, Inc. (Woodcliff Lake, NJ). https://www.cedengineering.com/userfiles/An%20Introduction%20to%20Condensers%20and%20Auxilary%20Equipment%20for%20Steam%20Power%20Plants%20R1.pdf, Accessed March 2021.

Haseli, Y., Dincer, I., and Naterer, G.F. (2008). Thermal effectiveness correlation for a shell and tube condenser with noncondensing gas. J. Thermophys. Heat Transf. *22*, 501–507.

Huang, L., Jiang, H., Wang, Y., Ouyang, Z., Wang, W., Yang, B., Liu, H., and Hu, X. (2020). Enhanced water yield of solar desalination by thermal concentrated multistage distiller. Desalination *477*, 114260.

Incropera, F., Dewitt, D., Bergman, T., and Lavine, A. (2007). Fundamentals of Heat and Mass Transfer, Sixth. (John Wiley & Sons).

Jarimi, H., Powell, R., and Riffat, S. (2020). Review of sustainable methods for atmospheric water harvesting. Int. J. Low Carbon Technol. *15*, 253–276.

Kim, K., Lee, Y., and Jeong, J.H. (2019). Dropwise condensation induced on chromium ion implanted aluminum surface. Nucl. Eng. Technol. *51*, 84–94.

Liu, Z., and Preston, D.J. (2019). Enhanced condensation for improved energy efficiency. Joule *3*, 1182–1184.

Nusselt, W. (1916). De oberflachenkondensation des waserdampfes. Z. VDI *541–546*, 569–575.

Panuthara, J.P., Muttathara, J.P.M., Ramachandralal, R.M., Asirvatham, L.G., and Wongwises, S. (2019). Experimental investigation of condensation heat transfer on chlorotriethylsilane coated grooved vertical tube. Int. Commun. Heat Mass Transf. *108*, 104312.

Pattanayak, L., Padhi, B.N., and Kodamasingh, B. (2019). Thermal performance assessment of steam surface condenser. Case Stud. Therm. Eng. *14*, 100484.

Phadke, M.S. (1989). Quality Engineering Using Robust Design (Prentice Hall).

Preston, D.J., Lu, Z., Song, Y., Zhao, Y., Wilke, K.L., Antao, D.S., Louis, M., and Wang, E.N. (2018). Heat transfer enhancement during water and hydrocarbon condensation on lubricant infused surfaces. Sci. Rep. *8*, 1–10.

Preston, D.J., Mafra, D.L., Miljkovic, N., Kong, J., and Wang, E.N. (2015). Scalable graphene coatings for enhanced condensation heat transfer. Nano Lett. *15*, 2902–2909.

Preston, D.J., Song, Y., Lu, Z., Antao, D.S., and Wang, E.N. (2017). Design of lubricant infused surfaces. ACS Appl. Mater. Interfaces *9*, 42383–42392.

Rose, J.W. (1988). Fundamentals of condensation heat Transfer : Laminar film condensation. JSME Int. J. *31*, 357–375.

Rungraeng, N., Yoon, S.H., Li, Y., and Jun, S. (2015). Development of a self-slippery liquid-infused porous surface (SLIPS) coating using carbon nanotube composite for repelling food debris and microbial biofilms. Trans. ASABE *58*, 861–867.

Schellenberger, F., Xie, J., Encinas, N., Hardy, A., Klapper, M., Papadopoulos, P., Butt, H.J., and Vollmer, D. (2015). Direct observation of drops on slippery lubricant-infused surfaces. Soft Matter *11*, 7617–7626.

Shi, Z., Xiao, Y., Qiu, R., Niu, S., and Wang, P. (2017). A facile and mild route for fabricating slippery liquid-infused porous surface (SLIPS) on CuZn with corrosion resistance and self-healing properties. Surf. Coat. Technol. *330*, 102–112.

Tanner, D.W., Potter, C.J., Pope, D., and West, D. (1965). Heat transfer in dropwise condensation-Part I the effects of heat flux, steam velocity and non-condensable gas concentration. Int. J. Heat Mass Transf. *8*, 419–426.

Tsuchiya, H., Tenjimbayashi, M., Moriya, T., Yoshikawa, R., Sasaki, K., Togasawa, R., Yamazaki, T., Manabe, K., and Shiratori, S. (2017). Liquid-infused smooth surface for improved condensation heat transfer. Langmuir *33*, 8950–8960.

Villegas, M., Zhang, Y., Abu Jarad, N., Soleymani, L., and Didar, T.F. (2019). Liquid-infused surfaces: a review of theory, design, and applications. ACS Nano *13*, 8517–8536.

Wang, N., Xiong, D., Pan, S., Deng, Y., and Shi, Y. (2016). Fabrication of superhydrophobic and lyophobic slippery surface on steel substrate. Appl. Surf. Sci. *387*, 1219–1224.

Wang, P., Huang, G., Chang, W., Alwazzan, M., Peng, B., Abdulshaheed, A.A., Zhao, Y., and Li, C. (2020). A laboratory scale heat pipe condenser with sweating boosted air cooling. Appl. Therm. Eng. *170*, 114915.

Wen, R., Xu, S., Ma, X., Lee, Y.C., and Yang, R. (2018). Three-dimensional superhydrophobic nanowire networks for enhancing condensation heat transfer. Joule *2*, 269–279.

Wong, T.S., Sun, T., Feng, L., and Aizenberg, J. (2013). Interfacial materials with special wettability. MRS Bull. *38*, 366–371.

Yang, H., Meng, N., and Li, T.L. (2019). Coupling effect of evaporation and condensation processes of organic Rankine cycle for geothermal power generation improvement. J. Cent. South Univ. *26*, 3372–3387.

Zhang, T.Y., Mou, L.W., Zhang, J.Y., Fan, L.W., and Li, J.Q. (2020). A visualized study of enhanced steam condensation heat transfer on a honeycomb-like microporous superhydrophobic surface in the presence of a non-condensable gas. Int. J. Heat Mass Transf. *150*, 119352.

iScience, Volume *24*

Supplemental information

Steam condensation heat transfer on lubricant-infused surfaces

Ryan Stoddard, Karthik Nithyanandam, and Ranga Pitchumani

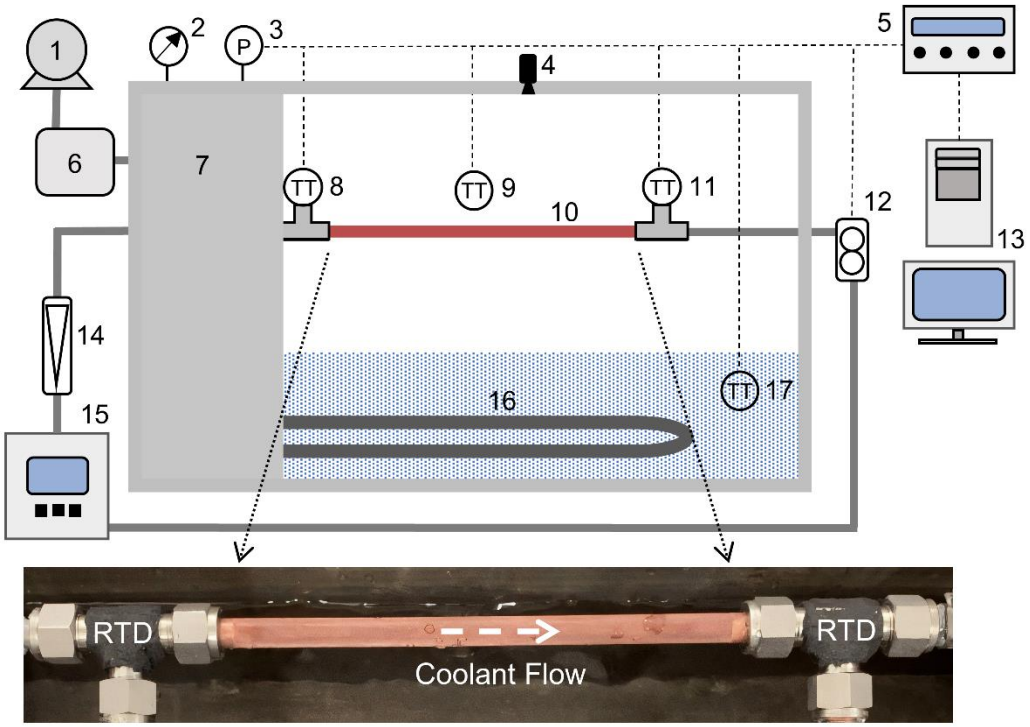

Figure S1. Schematic of condensation experimental setup with components and photo of mounted test section. 1-vacuum pump, 2-pressure gauge, 3-pressure transmitter, 4-borescope camera, 5-data acquisition, 6-cold trap, 7-vacuum chamber, 8-inlet RTD, 9-vapor RTD, 10-test section, 11-outlet RTD, 12-flow transmitter, 13-computer, 14-visual flowmeter, 15-chiller/recirculator, 16-immersion heater, 17-hotwell RTD. Related to Figure 4, Figure 5, Figure 6, Figure 10, Transparent Methods, Results and Discussion.

Table S1. Reported Instrumentation Precision Uncertainty

Related to Figures 4-6, Transparent Methods, Results and Discussion.

Measurement	Device	Reported Uncertainty / Resolution
T_{in}, T_{out}, T_v	RTD (class A)	0.06%; ± (0.15 + 0.002T)°C
$\dot{V}$	Omega FPR-200	2% of full scale (5 V)
D_i, D_o, L	Calipers	0.01 mm
h_i	Gnielinski correlation	10%

Table S2. Properties of Infused Lubricants

Related to Figures 4-11, Transparent Methods, Results and Discussion.

Lubricant	Density (g/ml)	Kinematic Viscosity (cSt @ 40°C)	Dynamic Viscosity (mPa-s @ 40°C)	Surface Tension (mN/m @ 23°C)
Krytox 101	1.89	7.8	14.7	10.3
Krytox 102	1.91	15.0	28.7	14.5
Krytox 103	1.92	30.0	57.6	15.9
Krytox 104	1.93	60.0	115.8	15.9
Krytox 105	1.94	160.0	310.4	16.1

Transparent Methods

Condensation experimental setup and procedure

The design and assembly of the steam condensation experimental setup is shown schematically in Figure S1, where the test section (10) was housed inside an aluminum vacuum chamber (internal dimensions of 50cm x 35cm x 30cm) with a top-mounted camera (4) for imaging. A 1000-Watt, adjustable temperature immersion heater (16) was used for steam generation in the hotwell of the vacuum chamber (7) and a vacuum pump (1) was used to control pressure in the chamber from atmospheric down to 5 kPa. Condensation heat transfer was investigated over the external surface of 20 cm-long, horizontally-mounted, thin-walled (0.81mm) tubes with outer diameter of 9.5 mm. After installation using compression fittings, a 16.7 cm length of the test section was exposed to the vapor environment inside the vacuum chamber.

A Cole-Palmer Polystat Cooling/Heating Recirculator (15) was used to drive deionized cooling water through the test section. The volumetric flow rate of the cooling water was controlled using presets on the recirculator and measured using an Omega FPR-200 series flow transmitter (12). Two resistance temperature detectors (RTD) were mounted inside insulated, Swagelok T-fittings to monitor flow temperatures at the inlet and outlet of the test section (8,11). Additionally, two RTDs were used to measure steam temperature (9) and hotwell water temperature (17) inside the vacuum chamber and an Omega PX-119 series pressure transmitter (3) was used to monitor vacuum chamber absolute pressure. All gauge measurements were acquired and displayed using National Instruments temperature (NI-9217) and multifunction (PXI-6221) input modules and LabView 2018 (5,13).

During a typical condensation experiment, the hotwell of the chamber was first filled to a depth of approximately 10 cm with distilled water and heated to a known temperature (40°C) using the immersion heater. The coolant water recirculator was started and allowed to stabilize at the desired coolant temperature and flow rate. Next, the chamber was sealed and evacuated to the saturation pressure of the hotwell water (~7.4 kPa), that corresponds to the typical vacuum conditions in water-cooled surface condensers. The hotwell water was then allowed to boil vigorously for approximately 30 minutes to remove any non-condensable gases from the water and chamber. Finally, as the chamber temperature and pressure were held constant, coolant temperature through the test section was adjusted and allowed to reach steady-state at desired conditions for experimental measurements. Steady-state at each ΔT_{LM} was determined by reference to test section inlet temperature stabilizing within 0.2°C of target inlet temperature for at least one minute. The inlet temperature of cooling water could be adjusted from 10°C to 40°C and was varied to take measurements across a ΔT_{LM} range of 2.5°C to 20°C. From start until finish, a typical condensation experiment lasted one hour.

Heat Transfer Data Reduction

The energy balance between the latent heat released by the condensing steam and the temperature increase of the coolant water was used to calculate the external condensation heat transfer coefficient. The heat transferred from the steam to the coolant water was assumed to be one-dimensional in the radial direction, neglecting both axial and circumferential variations in tube temperature. Additionally, the thermal resistance developed by the functionalizing agents were neglected in computing the condensation heat transfer coefficient on the exterior of the tube (h_c). Finally, although the cooling water temperature and heat transfer rate varied in the axial direction, only the surface-averaged heat transfer rate over the exposed 16.7 cm of the test section length was calculated since surface temperature measurements of the test section were not made.

The total heat transfer rate ($\dot{q}$) at steady state was computed based on the cooling water conditions, as given by

$$\dot{q} = \rho \dot{V} c_p (T_{out} - T_{in}) \qquad \text{(Equation 8)}$$

where ρ, $\dot{V}$, c_p, T_{in}, and T_{out} are the density, flow rate, specific heat capacity, inlet temperature and outlet temperature of the cooling water, respectively. The total resistance to heat transfer R_t was next calculated by dividing the logarithmic mean temperature difference (ΔT_{LM}) by $\dot{q}$, as given by

$$R_t = \frac{\Delta T_{LM}}{\dot{q}} \quad \text{(Equation 9)}$$

$$\Delta T_{LM} = \frac{(T_v - T_{out}) - (T_v - T_{in})}{ln\left(\frac{T_v - T_{out}}{T_v - T_{in}}\right)} \quad \text{(Equation 10)}$$

where T_v is the vapor temperature inside the vacuum chamber. Next, the Gnielinski convection correlation (Incropera, Dewitt, Bergman, and Lavine, 2007) for turbulent flow in circular tubes was used to calculate the internal convection heat transfer coefficient (h_i), as given by

$$h_i = \left(\frac{k_l}{D_i}\right)\frac{\left({}^{f}/_{8}\right)(Re - 1000)Pr}{1 + 12.7\left({}^{f}/_{8}\right)^{1/2}\left(Pr^{2/3} - 1\right)} \quad \text{(Equation 11)}$$

where D_i is the interior diameter of the test section and k_l, Re, and Pr are the thermal conductivity, Reynolds number and Prandtl number of the cooling water calculated at the average of inlet and outlet cooling water temperatures. The friction factor f in Equation 11 is given by the Petukhov correlation (Incropera, Dewitt, Bergman, and Lavine, 2007) factor for a smooth tube.

$$f = (0.790\, ln\, Re - 1.64)^{-2} \quad \text{(Equation 12)}$$

Next, the internal convection thermal resistance (R_i) and the conduction thermal resistance (R_m) due to the tube wall were calculated.

$$R_i = \frac{1}{2\pi r_i L h_i} \quad \text{(Equation 13)}$$

$$R_m = \frac{ln\left(\frac{r_o}{r_i}\right)}{2\pi L k_m} \quad \text{(Equation 14)}$$

where r_i and r_o are the inner and outer radii of the tube, respectively, L is the length of test section exposed to the inside of the vacuum chamber and the thermal conductivity of copper (k_m) was assumed constant at 0.385 kW/m°C (Incropera, Dewitt, Bergman, and Lavine, 2007). The external thermal resistance to heat transfer (R_e) was then calculated by subtracting R_i and R_m from R_t and converted to an external condensation heat transfer coefficient (h_c), as given by

$$R_e = R_t - R_i - R_m \quad \text{(Equation 15)}$$

$$h_c = \frac{1}{2\pi r_o L R_e} \quad \text{(Equation 16)}$$

Experimental Uncertainty Analysis

The data collection algorithm for the condensation heat transfer experimental setup was designed to collect and store batches of data at regular time intervals. In order to realize statistical significance in the data, it was important that these data batches were of adequate size to minimize random error, while also staying small enough to provide real-time indications of experimental conditions for the operator. As such, an analysis was conducted for sample size (*N*). The direct measurement device in the experimental setup that produced the largest sample variance was the flow transmitter, so this device was used for computation

of needed sample size. The signal recorded by LabView from the flow transmitter was voltage, which was multiplied by the appropriate calibration factor to realize a measurement of volumetric flow rate in liters per minute. Using the data from calibration runs of the flow transmitter at the highest experimental flowrate shows the following: N = 120 samples; sample mean x = 3.11V; and sample variance s^2 = 0.00447V^2.

$$N = \frac{s^2 t^2_{120;\,0.025}}{Error^2} \quad \text{(Equation 17)}$$

In order to assure 95% confidence normalized random errors of 0.5% or less in the mean, the t-distribution value (t = 1.98) for 120 samples was used in Equation 18 to obtain $N \geq 73$ as a minimum sample size. Recalculating Equation 17 using a t-distribution value (t = 1.995) for 75 samples yields $N \geq 74$ as a minimum sample size. During experiments, a sample size of N = 80 was used for each data batch. In experimental runs, each data point collected consisted of a mean and variance from a data batch of 80 samples taken over a 15 second time period. Hence, a measurement that averaged 10 data points taken at steady-state conditions consisted of 800 total samples.

Each measurement taken during experimentation involved two types of random error: statistical uncertainty (u_s) associated with the 80-sample batches and instrument precision uncertainty (u_i) as noted in Table S1. Statistical uncertainty is a Type A uncertainty and instrument precision uncertainty is a Type B uncertainty (Taylor and Kuyatt, 1994), and they combine to give an overall uncertainty for each experimental parameter in each data batch.

$$u = \sqrt{u_s^2 + u_i^2} \quad \text{(Equation 18)}$$

Statistical uncertainty (u_s) is a function of sample variance (s^2), number of samples (N) and the desired confidence interval from the t-distribution, as given by:

$$u_s^2 = \frac{s^2 t^2_{n;\,\alpha}}{N} \quad \text{(Equation 19)}$$

As expected, statistical uncertainty decreases as the number of samples increases. Since the instrument errors given in Table S1 represent expected lower and upper limits for an obtained measurement, they are taken to represent a rectangular (uniform) distribution (Taylor and Kuyatt, 1994), giving uncertainty:

$$u_i = \frac{E}{\sqrt{3}} \quad \text{(Equation 20)}$$

Rearranging Equation 18 and choosing N = 80 and t = 1.995 for 95% confidence yields the following uncertainty result for each of the experimental measurements:

$$u = \sqrt{0.053 s^2 + \frac{E^2}{3}} \quad \text{(Equation 21)}$$

where s^2 is the variance of the 80-sample batch and E is the reported instrument error shown in Table S1.

Since the goal of this work was to investigate average heat transfer coefficients under steady state conditions, several data batches were combined to yield time-averaged values of experimental measurements and uncertainties, as given by:

$$\bar{x} = \frac{\sum_{j=1}^{k} N_j x_j}{\sum_{j=1}^{k} N_j} \quad \text{(Equation 22)}$$

$$u(\bar{x}) = \frac{\sum_{j=1}^{k} N_j[u_j^2 + (\bar{x} - x_j)^2]}{\sum_{j=1}^{k} N_j} \quad \text{(Equation 23)}$$

Combining k data batches using Equations 22 and 23 yielded the experimental measurements and uncertainties that were reduced using Equations 8–16.

Thermodynamic properties of the coolant water were assumed exact for calculation purposes. Additionally, area calculations of the test section were assumed exact since the maximum uncertainty of 0.01 mm for measurement calipers produced measurement variation of 0.19% for cross-sectional area and 0.10% for surface area. All of these uncertainties are negligible when compared to other experimental uncertainties.

All experimental measurements were independent, so there were no covariances between variables. Once the experimental measurements and uncertainties were calculated, quantities of interest, such as mass flow rate, heat transfer, resistances to heat transfer, and ultimately convection heat transfer coefficients could be calculated using Equations 8–16, and associated uncertainties were calculated using algebraic propagation of uncertainty techniques (Taylor and Kuyatt, 1994).

Test Section Surface Modification

As-purchased, copper tubing was cut to appropriate length, then scoured with a brass-bristled brush, and subsequently cleaned in acetone and methanol to remove natural oxides and organics. Next, the tube was rinsed thoroughly with deionized water and dried before texturing the surface either by chemical etching or electrodeposition.

Etched copper test sections were prepared by first masking each end of the tube and covering the inlet and outlet with plastic caps. These steps were taken to preserve a tight fit into the compression fittings of the condensation test apparatus and avoid inadvertent modification to the smooth inside finish of the tube. Next, the masked tube was submerged in a 1:1 mixture of 3% hydrogen peroxide and 12M hydrochloric acid for 20 minutes. Once etching was complete, the tube was rinsed thoroughly with deionized water and lightly brushed to remove residue.

Electrodeposited copper test sections were prepared using one of four different overpotentials – 0.5V, 0.6V, 0.7V or 1.1V – in a two-step electrodeposition process. After masking and capping one end of the tube, the tube was lowered into an electrolyte comprised of 1 mol/L $CuSO_4$ and 0.5 mol/L H_2SO_4. The test section served as the working electrode while a concentrically placed copper tube served as the reference electrode for electrodeposition. The first electrodeposition step was conducted at constant overpotential of 0.5 V, 0.6 V, 0.7 V or 1.1 V for five minutes. After a brief rinse with deionized water, the test section was returned to the electrolyte. The second electrodeposition step was conducted at constant current of 0.75 A for approximately nine minutes to achieve a charge transfer of 7.5 C/cm^2. This step strengthened the initial, rough coating electrodeposited during the first step. A Zeiss 1550 field-emission scanning electron microscope (FESEM) was used to characterize the microscale morphologies of the various texturing methods and the surface roughness profiles were characterized using a Dektak XT stylus profilometer. FFT analysis was conducted using Matlab (MATLAB, 2020).

Surface Functionalization

Five different functionalizing agents were tested in this study: octylphosphonic acid, n-Hexadecyl Mercaptan (mercaptan), 1H,1H,2H,2H-Perfluorodecyltriethoxysilane (silane), stearic acid, and Sylgard-184.

The application techniques for mercaptan, octylphosphonic acid, and stearic acid were nearly identical. First, each substance was diluted to 0.02 mol/L concentration in alcohol. Ethanol was used as the solvent for mercaptan, while methanol was used as the solvent for octylphosphonic acid and stearic acid. A test section was submerged in the respective functionalizing agent for one hour with plastic caps covering both

ends of the test section to avoid treatment of the smooth, inner surface of the tube. Functionalization was conducted at room temperature (~22°C) for octylphosphonic acid and stearic acid, and at 60°C for mercaptan. Finally, the test section was removed from the functionalizing agent, rinsed with either ethanol or methanol, depending on the solvent of the functionalizing agent, and allowed to air dry at room temperature for at least one hour.

Silane was applied to test sections from aqueous alcohol. First, the silane solution was prepared using 90% ethanol, 8% deionized water, 2% silane, and a few drops of acetic acid to lower the mixture pH to approximately 5.5 (Arkles, 2014). The test section was capped on both ends and placed in the silane solution for 5 minutes. After removal, the test section was rinsed with ethanol and allowed to air dry for approximately 15 minutes. Then, a second 5-minute silane immersion was conducted after which the test section was cured at 110°C for 10 minutes.

Sylgard-184 is a highly viscous, two-part, polydimethylsiloxane elastomer. To functionalize a test section, the elastomer base was first diluted 10:1 using ethanol and mixed ultrasonically for three minutes. Next, the elastomer curing agent was added to the base mixture and stirred for 10 minutes. Application of the Sylgard-184 mixture to the test section was accomplished by first capping one end of the test section and dipping it into the mixture. After removal from the mixture, the test section was immediately spun at approximately 1700 rpm for 15 seconds to centrifugally remove excess diluted Sylgard-184 from the surface. Finally, the Sylgard-184 coated test section was cured at 165°C for 10 minutes.

Lubricant Infusion

Lubricant infusion was the third step in test section preparation. After texturing and functionalization, the test section was weighed to determine an uninfused mass as a baseline. Five different Krytox lubricants were used for infusion during this study. Krytox lubricants are perfluoropolyether (PFPE) oils with specific gravities greater than unity. Table S2 shows the properties of the five lubricants used. Next, one of the lubricants was dripped onto the surface of the test section and spread evenly across the surface using a compressed air stream. The resulting lubricant-infused surface was placed at a 30° angle for at least 12 hours, allowing excess lubricant to drain from the test section before testing. Liquid infused surfaces are conventionally characterized in terms of the static contact angle and contact angle hysteresis of a water droplet on the surface.

Static water contact angle and contact angle hysteresis were measured using a contact angle goniometer (ramé-hart Model 190). The measurements were made at ambient pressure and temperature conditions by placing a 10 microliter droplet of deionized water on the fabricated surfaces. All the functionalized liquid infused surfaces exhibited contact angles in the range 111.6–128.3°, with most in the range $120 \pm 2°$. For reference, the contact angle on an unfunctionalized liquid infused surface was measured to be $104 \pm 2°$.The contact angle hysteresis values were all less than 5°. Although the contact angle and the contact angle hysteresis are normally used to describe the non-wetting characteristics of the surfaces in the literature, since the present study was conducted in a vacuum environment, whereas the contact angles were all measured at ambient conditions, these parameters were less relevant to the reported condensation heat transfer characteristics (Drelich, Boinovich, Chibowski, Della Volpe, Hołysz, Marmur, and Siboni, 2020; Schrader, 1974). On the other hand, the surface asperity structural parameters of mean peak asperity spacing and asperity height discussed in Figures 1–2 were the more significant parameters as presented in Figures 4–9.

Supplemental References

Arkles, B., 2014. Silane Coupling Agents Connecting Across Boundaries, Gelest, Inc.

Drelich, J.W., Boinovich, L., Chibowski, E., Della Volpe, C., Hołysz, L., Marmur, A., Siboni, S., 2020. Contact angles: History of over 200 years of open questions. Surf. Innov. 8, 3–27. https://doi.org/10.1680/jsuin.19.00007

Incropera, F., Dewitt, D., Bergman, T., Lavine, A., 2007. Fundamentals of Heat and Mass Transfer, Sixth. ed. John Wiley & Sons.

MATLAB, 2020. Version 9.10 (R2020a).

Schrader, M.E., 1974. Ultrahigh vacuum techniques in the measurement of contact angles. III. Water on copper and silver. J. Phys. Chem. 78, 87–89. https://doi.org/10.1021/j100594a017
Taylor, B.N., Kuyatt, C.E., 1994. Guidelines for Evaluating and Expressing the Uncertainty of NIST Measurement Results, Technical Note 1297.